Check for updates

Investigation of the Filling of a Spherical Pore Body with a Nonwetting Fluid: A Modeling Approach and Computational Fluid Dynamics analysis

Amgad Salama[1] · Jisheng Kou[2,3] · Shuyu Sun[4] · Mahmoud Hefny[5]

© The Author(s) 2024

Abstract

Understanding the dynamics of the filling process of a pore body with a nonwetting fluid is important in the context of dynamic pore network models and others. It can justify many of the assumptions behind the different rules that describe how the network behaves during imbibition and drainage processes. It also provides insight into the different regimes pertinent to this system. The filling process starts with the contact line pinning at the pore entrance. Three regimes can be identified during the filling process that is related to how the contact line advances. In the first two regimes, the contact line pins at the pore entrance while the emerging droplet develops, and in the third one, the contact line departs the entrance of the pore and advances along the pore surface. During the first regime, which is brief, the curvature of the meniscus increases, and likewise, the corresponding capillary pressure, while in the other two regimes, the curvature decreases and so does the capillary pressure. Such behavior results in the rate at which the nonwetting fluid invades the pore to change. It initially decreases, then increases as the meniscus advances. The radius of curvature of the meniscus, eventually, increases to infinity for which the interface assumes a flat configuration. A one-dimensional modeling approach is developed that accounts for all these regimes. The model also considers the two immiscible fluids over a wide spectrum of contrast in viscosity. Information about the mean velocity of the invading fluid, the location of the contact line, the radius of curvature of the meniscus, the volume of the emerging droplet, and several others are among the details that the model provides. A computational fluid dynamics (CFD) simulation has also been considered to confirm the proposed fates of the interface and to provide a framework for comparisons. The results of the validation process show, generally, a very good match between the model and the CFD analysis.

1 Introduction

Our understanding of the world we live in comes at different levels of resolutions. If we are interested in viewing small-scale details, we focus our attention and vision on the features of interest and this comes at the expense of reducing the field of view and vice


Extended author information available on the last page of the article

versa. The interesting thing, however, is that every level of detail envisions seemingly different realities that sometimes look contradicting. For example, focusing on a small volume of a fluid reveals the discrete nature of the material with molecules, looking like billiard balls, wandering in all directions in the empty space surrounding them. If we defocus our vision and increase the field of view, we no longer see individual molecules in the empty space, rather we see a continuum filling the space with no individual molecules or gaps between them. During the focusing/defocusing processes, the resolution changes between sharp and blurred views indicating that there are areas where neither the level of focusing nor the field of view are sufficient to capture meaningful details. One, therefore, may think of two length scales, the first is the length scale associated with the feature of interest and the second is that associated with the field of vision, with the latter much larger than the former. Porous material is an interesting example that can provide three levels of detail (Whitaker 1999; Hornung 1997; Das and Hassanizadeh 2005; Salama and Geel 2008; Salama and Geel 2008; El-Amin et al. 2011). These are the molecular scale, the pore scale, and the continuum scale. Each scale is characterized by its own variables that are linked across the scales via integral operations. On moving from one scale to the other, variables need to be cast in a way that make them suitable for analysis and measurements. As an example, at the molecular scale, both the velocity and the position are associated with the particles, i.e., $\mathbf{v}_p = \mathbf{v}_p(t)$ and $\mathbf{x}_p = \mathbf{x}_p(t)$, where $\mathbf{v}_p$ and $\mathbf{x}_p$ are the velocity and the position of the particle p, which are both functions of the time, t. At this scale, one solves only for primitive variables (e.g., position and velocity of the particles) and other variables and material properties (e.g., pressure, density, viscosity, thermal conductivity) do not appear in the equations. They can only be obtained via postprocessing operations of the primitive variables. Despite the simplicity of this approach, they require large computing resources and can only apply to very small-scale domains. At the fluid continuum scale, on the other hand, the velocity is no longer associated with the particles, and in the Euler description it is a function of the position and time, $\mathbf{v} = \mathbf{v}(\mathbf{x}, t)$. The advantages of this approach are that one no longer needs to follow individual particles and it becomes possible to investigate relatively larger size domains. However, other variables and media properties relevant to the continuum description need to be evaluated by either experimentally or solving closure problems for a representative unit cell at the molecular scale. Similarly, at the porous media continuum scale, such a velocity is a function of the position and time, and in this case, it does not matter whether the position happens to be in the fluid or the solid regions. This is, in fact, a huge simplification given the difficulty in constructing a geometrical realization of real porous medium. It is noteworthy that on doing upscaling, we can retrieve the upscaled variable from their small-scale counterparts via averaging or homogenization operations. However, this process also generates macroscopic variables that do not have counterparts at a large scale. They must be modeled by solving closure problems over representative periodic unit cells (Mei 1992; Hornung 1997; Wood et al. 2003; Buckinx and Baelmans 2015; Chabanon et al. 2017; Bowen Ling and Battiato 2020). An obvious example of this may be stated in the realm of turbulent flows when extra terms appear in the Reynolds-averaged Navier–Stokes equation representing extra stresses (Castro and Vanderwel 2022; Salama 2021a). In many situations, such terms are modeled by implementing new properties that relate fluxes and gradients. Some of these properties represent intrinsic characteristics of the medium and some others are phenomenological. These properties can either be measured or obtained via small-scale modeling. It is to be noted that such upscaling processes, which aim at simplifying the analysis of otherwise complex systems, can be utilized in different contexts, e.g., (Salama et al. 2017a).

Sometimes measuring intrinsic properties can be very difficult, particularly in extreme conditions. For example, measuring the permeability of a sample of a tight formation would require specialized instruments that are suited to withstand extreme pressures, which may not be readily available except at specialized laboratories (Salama et al. 2017b). However, using upscaling theories may allow us to determine such properties following the simulation of the flow in a representative volume of the formation. This, on the other hand, requires that we build a realization of the internal structure of the sample such that a reliable pore-scale simulation is possible, which has been recently possible using computer tomography. This approach requires that the internal space of the realized sample is discretized such that computational fluid dynamics analysis may be conducted to retrieve macro-scale properties (Mohammadmoradi and Kantzas 2016; Silin et al. 2011; Hilpert and Miller 2001; Piller et al. 2009). The complexity of this approach is clear, particularly when considering complex phenomena, e.g., multiphase flows at the pore scale. On the other hand, based on our understanding of the processes involved at the pore scale, it has been realized that the hierarchy of scales associated with a representative porous medium sample can be categorized into two main groups, namely pore throats and pore bodies. Along the pore throats, the pressure mainly drops while staying almost constant along the pore bodies. In other words, if it is possible to transform a real porous medium sample into a set of pore bodies of various sizes connected with pore throats, then it may be possible to analyze this system in a simpler way (Thompson 2002; Joekar-Niasar and Hassanizadeh 2012; Joekar-Niasar et al. 2012; Zhang et al. 2025; Ryazanov et al. 2009; Cui et al. 2022). Figure 1 shows a CT scan of a sample porous medium and an equivalent pore network that could represent its essential features.

Such a kind of transformation allows the possibility of using simplified pressure drop formulas (e.g., the Hagen–Poiseuille equation) to calculate the overall pressure drop across the sample from which an estimation of the permeability may be obtained. Furthermore, instead of going through detailed CFD simulation of multiphase
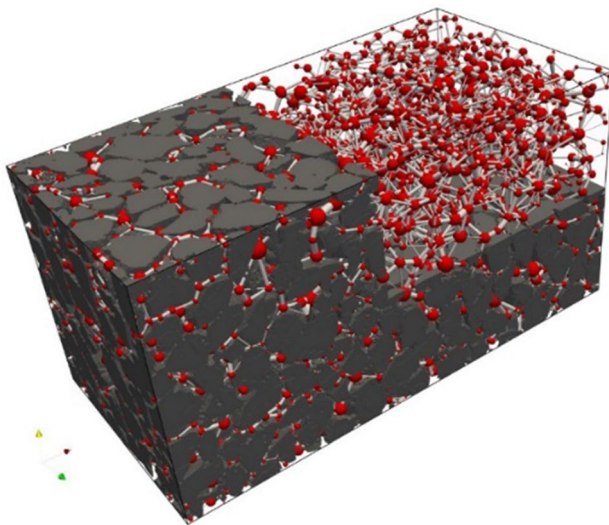
Fig. 1 A realization of a porous medium sample with its equivalent pore network. The pore network consists of pore bodies and pore throats of different sizes, (quoted from (Hefny et al. 2020))

systems in real porous medium samples, a simplified methodology based on identifying entry pressure thresholds for every pore throat may be used to quantify the displacement of one phase by another immiscible one over the network. Typical imbibition and drainage processes in such networks follow preset rules that are determined based on our understanding. The success of a given pore network in representing a real porous medium sample depends on how the geometrical and topological features are accounted for. The geometric properties of the porous media, such as the locations of the pores and throats, along with their respective size distributions, represent key parameters in constructing a representative pore network (Bryant and Blunt 1992; Knackstedt et al. 1998). Most of the early works on pore network modeling assumed that the throats were cylinders of negligible volume. Pore bodies, on the other hand, were either not modeled, or were assumed spherical, cubical or cylindrical in shape (Bryntesson 2002; Jivkov and Xiong 2014; Laudone et al. 2008; Meyers and Liapis 1999; Meyers et al. 2001), while in multiphase flow applications, it may be necessary to pay specific attention to the local morphology of the throats (Fenwick and Blunt 1998; Gao et al. 2012; Hui and Blunt 2000; Man and Jing 1999), in others, such as permeability or diffusivity determinations, pore throats may be considered as straight channels with locally averaged cross sections. In addition, the models have to reflect basic topological properties, such as average pore coordination number and spectrum, which have been studied in several works (Meyers and Liapis 1999; Raoof and Hassanizadeh 2010). Three basic methods to construct a PNM may be highlighted. In the first, a statistically equivalent network may be constructed based on the distributions of basic morphologic parameters (Adler and Thovert 1998; Ioannidis and Chatzis 2000; Levitz 1998; Roberts and Torquato 1999; Yeong and Torquato 1998). Such a constructed network would be equivalent to the real system only in a statistical sense. In the second approach (Piri and Blunt 2005), a one-to-one mapping between the real structure of the porous medium and the corresponding PNM is established as depicted in Fig. 1. The third approach is called the grain-based approach, in which a randomly packed network of initially equallysized spheres is constructed. The spheres are then allowed to expand and sometimes overlap. Compaction was modeled by moving the centers of the spheres closer together. Other versions of this approach have been developed, [e.g., Pilotti (2000), Oren and Bakke (2002)].

When the pressure difference along the network system is larger than the critical entry pressure, the meniscus advances along the pore throat and directly into filling the pore body. In the realm of quasistatic pore network modeling, this may be sufficient to investigate the invasion process of the network with the nonwetting fluid. However, such analysis sheds no light on the dynamics of the filling process, the time it takes to invade the whole pore body, the distribution of the pressure along the system, and the flow rate associated with the invasion process. This is the focus of this research in which we develop a simplified modeling approach that describes the filling process and how the meniscus advances inside the pore. Furthermore, a computational fluid dynamics analysis of this system has been conducted to provide a framework for verification and validation and to confirm the fates of the meniscus along the system.

This paper is organized as follows: in the next section a discussion on where this work lays in arena of other works on pore network modeling and why is it important, we then introduce derivation to the one-dimensional model, following we introduce the CFD analysis constructed to provide a framework for validation of the developed model, and finally a more discussion on the model predictions is provided.

2 Problem Statement

The population of the pore network with one fluid by displacing the other immiscible one follows a predefined set of rules that are set according to our understanding of the processes and the specificity of the network topology. Two approaches have been adopted, namely (1) the quasistatic PNM and (2) the dynamic PNM. Quasistatic PNMs stem with a number of simplifying assumptions that are, largely, related to whether one needs to incorporate pore bodies in the analysis of the network or not. In the analysis of most quasistatic PNMs, pore bodies are usually neglected on account to their very little contribution to the pressure drop. Furthermore, in the invasion of the network by immiscible fluids, once the meniscus reaches the entrance of the pore, it directly proceeds to fill the pore body on account of the fact that the capillary pressure across the meniscus continuously decreases as it advances through the pore. In dynamic PNM, on the other hand, this may not be the case and the pore bodies constitute by large most of the storage capacity of the network and must, therefore, be incorporated in the saturation equation. During drainage processes, the nonwetting phase invades a pore throat when the capillary pressure in the pore throat is greater than the entry pressure. Different forms of capillary pressure have been proposed in the literature. For example, Thompson (2002), for the case of a cuboidal pore body, used a capillary pressure formula that first increases and then becomes a constant after the radius of the nonwetting phase bubble equals the radius of the inscribed circle of the square cross section of the largest connected throat. Joekar-Niasar et al. (2010), on the other hand, assumed a monotonic function for the capillary pressure, where it is approximately a constant beyond the entrance region. They also compared various forms of capillary pressure and concluded that the different forms have a negligible impact on the overall fluid–fluid displacement patterns.

It is interesting, however, to realize that the capillary pressure along the pore body continuously changes. It initially increases once the meniscus has reached the entrance of the pore, then continuously decreases as the meniscus advances, and eventually reaches zero when the meniscus assumes a flat surface. Understanding these fates is important in order to correctly model this system. Figure 2 shows a schematic of the different stages of the meniscus as the
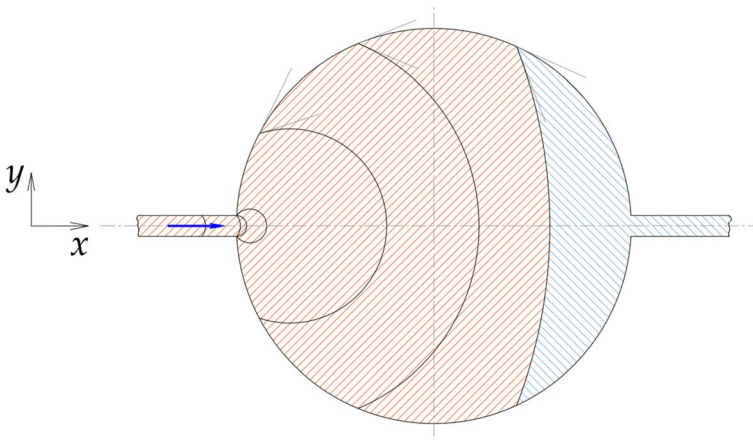
Fig. 2 The development of the meniscus inside the pore body. The radius of curvature briefly decreases at first then sharply increases to infinity as the meniscus advances inside the pore

nonwetting fluid advances inside the pore body from which it is apparent that the radius of curvature of the meniscus initially decreases and then continuously increases.

It is, therefore, interesting to depict such behavior based on a more elaborate framework to highlight the essence of this process. In this work, we develop a 1D modeling framework that describes the dynamicity of this process along the different stages of the interface development. Despite the fact that pore-scale analysis of the filling process of a pore body with a nonwetting fluid is by itself an interesting phenomenon worth investigation, it may also be important to highlight its relevance to dynamic pore network models. In dynamic pore network models, the capillary pressure is calculated, for example, based on an exponentially related capillary pressure function of the saturation in addition to some geometrical parameters (Yin et al. 2019). These models, however, do not consider the initial increase in the capillary pressure once the meniscus has reached the entrance, which may, arguably, be considered in the context of calculating the entry pressure value of each pore throat. In this work, however, the calculations of the flux are based on a real-time record of the meniscus location and curvature. It accounts for the three stages of the growth of the interface, which affects the flux calculations. Furthermore, the onset of the pinning and movement of the contact line along the pore body profile has been clearly identified, which, to the authors' knowledge, has not been clearly stated before.

In this work, we also introduce a CFD analysis to confirm the different fates and to provide a framework for the validation and verification of the developed model. The model can predict the time variation of the volume of the emerging droplet inside the pore, the location of the contact line, the flow rate variations with time, the capillary pressure, and the radius of curvature of the meniscus are among the variables of interest that can be monitored in this work.

3 A 1D Modeling Approach

In this section, the derivation of the 1D model is presented. The assumptions pertinent to this model is that it is a quasistatic model, the pore throats are cylindrical in shape, the pore body is spherical, gravity is ignored, and the viscosities of the two immiscible fluids are different.

3.1 Derivation

Consider the system shown in Fig. 3, which represents a pore body connected to two pore throats (tubes). The two tubes connected to the pore could be of the same or different diameters. A nonwetting fluid is forced to enter the left-hand side tube by applying external pressures at the inlet and the exit section of the system. Ignoring the local losses at the entrance and exit of the pore body, the single-phase flow equation in a tube, ignoring the inertia, which may only be effective at the very early time at the start of the flow (Ioannidis and Chatzis 2000), may be written as

$$-\frac{\partial p}{\partial x} + \mu \frac{1}{r}\frac{\partial}{\partial r} r \frac{\partial u}{\partial r} \pm \rho g = 0 \tag{1}$$

where r is the radius of the tube, p is the pressure, $u(r)$ is the velocity, g is the gravity, ρ, and μ are the density and viscosity of the invading fluid, respectively.

Ignoring the gravity and using the parabolic velocity profile $u = 2U\left(1 - r^2/R_t^2\right)$, where U is the mean velocity, the above equation reduces to
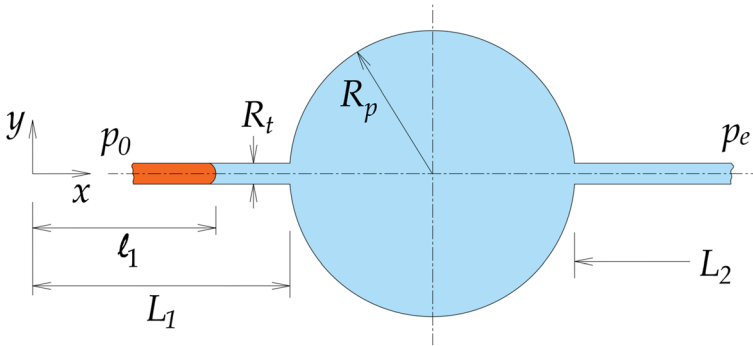
Fig. 3 Schematic representation of the considered system in which a spherical pore of radius R_p is connected to two cylindrical tubes of radius R_t. The length of the left-hand side tube is L_1, and that of the right-hand side is L_2

$$-\frac{\partial p(x)}{\partial x} + 8\mu \frac{U(t)}{R_t^2} = 0 \tag{2}$$

where R_t is the radius of the capillary tube. Integration of Eq. (2) over a control volume gives $\int_V \left[-dp(x)/dx + 8\mu U(t)/R_t^2 \right] dV = 0$. Since all the terms are only functions of x, the volume integration reduces to an integration along the tube length and one obtains

$$-\int_x dp + 8\mu \int_x \frac{U}{R_t^2} dx = 0 \tag{3}$$

In the case when two immiscible phases exist in the tube, integration over each phase and summation yields

$$-\left[\int_0^{\ell_1} dp + \int_{\ell_1}^{L_1} dp \right] + 8\frac{U}{R_t^2}\left[\mu_1 \int_0^{\ell_1} dz + \mu_2 \int_{\ell_1}^{L_1} dz \right] = 0 \tag{4}$$

Substitutions yields

$$-\left[\left(p_{\ell_1}^- - p_0 \right) + \left(p_{L_1} - p_{\ell_1}^+ \right) \right] + 8\frac{U}{R_t^2}\left[\mu_1 \ell_1 + \mu_2 (L_1 - \ell_1) \right] = 0 \tag{5}$$

Introducing the viscosity ratio $\lambda = \mu_1/\mu_2$ and substitution in Eq. (5) yields

$$\left(p_0 - p_{L_1} \right) - \left(p_{\ell_1}^- - p_{\ell_1}^+ \right) + 8\frac{U}{R_t^2}\mu_2\left[\lambda\ell_1 + (L_1 - \ell_1) \right] = 0 \tag{6}$$

Knowing that the capillary pressure across the meniscus is $p_c = p_{\ell_1}^- - p_{\ell_1}^+$, substitution in Eq. (6) yields

$$\left(p_0 - p_{L_1} \right) - p_c + 8\frac{U}{R_t^2}\mu_2\left[(\lambda - 1)\ell_1 + L_1 \right] = 0 \tag{7}$$

When the meniscus in the tube reaches the inlet to the pore, we have $\ell_1 = L_1$ and the whole tube becomes filled with the nonwetting fluid. In this case, Eq. (7) becomes

$$p_0 - p_{L_1} + 8\frac{U}{R_t^2}\mu_1 L_1 = 0 \tag{8}$$

The volume flow rate in the tube is $U = Q/A$, and substitution in Eq. (8) yields the Hagen–Poiseuille's equation as

$$p_0 - p_{L_1} + \frac{8\mu_1 L_1 Q}{\pi R_t^4} = 0 \tag{9}$$

The flow rate exiting the tube equals negative that entering the pore; in other words, we have

$$Q = -dV/dt \tag{10}$$

Substitution in Eq. (9) yields

$$p_0 - p_{L_1} - \frac{8\mu_1 L_1}{\pi R_t^4}\frac{dV}{dt} = 0 \tag{11}$$

Ignoring the head loss in the pore body, the pressure at the inlet of the pore is related to that at the exit of the right-hand side tube as

$$p_{L_1} = p_c + \Delta p_{\text{exit}} + p_e \tag{12}$$

Likewise, the pressure drop along the right-hand side tube may be written as

$$\Delta p_{\text{exit}} = \frac{8\mu_2 L_2}{\pi R_t^4}\frac{dV}{dt} \tag{13}$$

Substitution of Eqs. (12) and (13) into Eq. (11) yields,

$$\left(\lambda L_1 + L_2\right)\frac{8\mu_2}{\pi R_t^4}\frac{dV}{dt} = \left(p_0 - p_e\right) - p_c \tag{14}$$

This ordinary differential equation (ode) is the governing law that describes the dynamics of this system. The capillary pressure across the meniscus in the pore may be calculated as $p_c = 2\gamma/R_m$, where γ is the interfacial tension and R_m is the radius of curvature of the meniscus. From Eq. (14), the rate of change of the volume of the nonwetting fluid in the pore is related to the capillary pressure update.

3.2 Determination of the Capillary Pressure

The capillary pressure in Eq. (14), along with the external pressures, represents the terms that drive the dynamics of the interface inside the pore. With the external pressure set constant, the capillary pressure must be updated as the interface advances inside the pore. Three regimes can be identified as the interface develops. In the first two regimes, the contact line pins at the entrance of the pore while developing, the meniscus assumes and in the third regime, the contact line moves along the surface of the pore. In the first regime (regime I, Fig. 4), which is essentially brief, the radius of curvature decreases until

Fig. 4 The interface develops inside the pore in three regimes. In regime I, the contact line pins at the entrance of the pore while the radius of curvature of the developing meniscus decreasing. In regime II, the contact line continues to pin at the pore entrance while its radius of curvature increases. In regime III, the contact line starts to depart the entrance of the pore moving along the surface of the pore
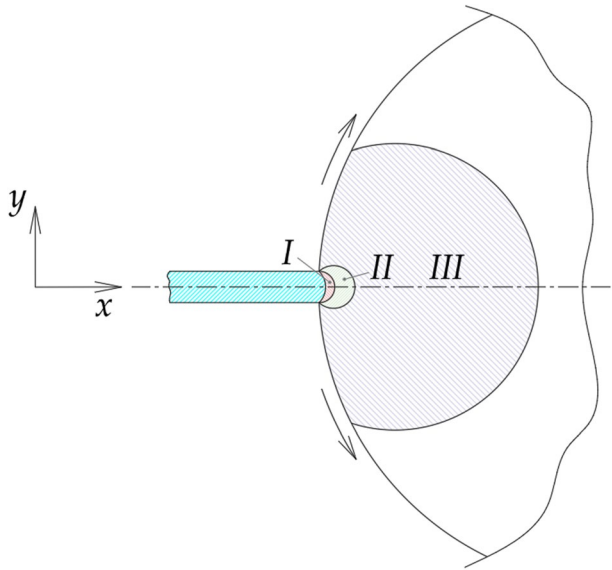

Table 1 Formulas for calculating the volume of the spherical cap in regions I and II

		Volume
Region I	$\vartheta_s \geq \vartheta \geq 0$	$V = \frac{\pi}{3}R_t^3 \left(\frac{2-3\sin\vartheta+\sin^3\vartheta}{\cos^3\vartheta} \right)$
Region II	$0 \leq \vartheta \leq \tan^{-1}\frac{dy}{dx} - \vartheta_s$	$V = \frac{\pi}{3}R_t^3 \left(\frac{2+3\sin\vartheta-\sin^3\vartheta}{\cos^3\vartheta} \right)$

it becomes equal to the radius of the tube with the contact angle changing. In this case, the capillary pressure increases and the flow rate drops. As the nonwetting fluid continues to invade the pore body, its volume increases and the radius of curvature starts to increase leading to a decrease in the capillary pressure and an increase in the flow rate. Yet the contact line still pinning at the tube exit. This marks region II which lasts until the contact angle between the meniscus and the surface of the pore becomes equal to the static contact angle at which time the contact line starts to move along the surface of the pore.

The contact line continues to move thereafter until it reaches the exit of the pore. This marks regime III along which the radius of curvature increases sharply toward infinity implying a flat interface. During this regime, the capillary pressure decreases until it becomes zero when the interface becomes flat. These regimes are depicted schematically in Fig. 4. The radius of curvature of the meniscus can be updated knowing the volume of the emerging droplet. This can be done according to the three previously defined regimes. In regimes I and II, the meniscus assumes a spherical cap with its volume calculated as given in Table 1. Figure 5a shows a schematic of the emerging droplet along with the essential parameters associated with regimes I and II.

In these two formulas, R_t is the radius of the capillary tube. It is noteworthy that the contact angle (ϑ) in these two regimes develops with time and is measured with respect to the wall of the capillary tube as depicted in Fig. 5a. As the contact line starts to move along the spherical pore wall, it maintains the static contact angle with the tangent to the pore profile, which changes along the pore. Figure 5b and c show schematic of the meniscus as
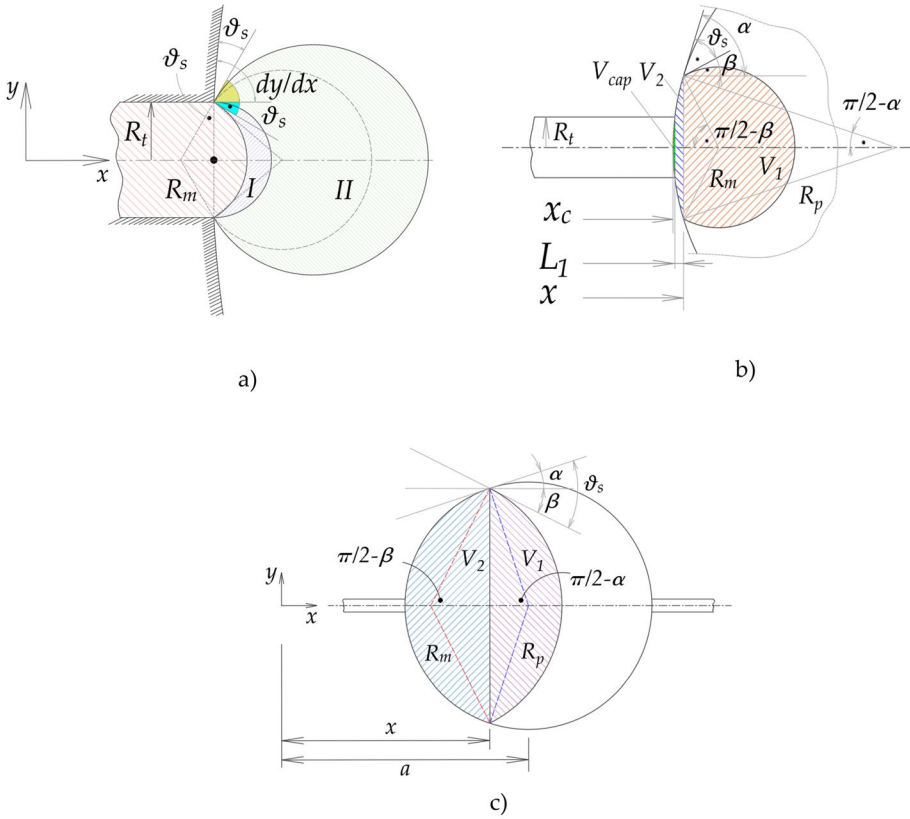
Fig. 5 Schematics of the emerging droplet at different stages with all the geometric parameters relevant to this system displayed

it develops. The volume of the emerging droplet can be divided into two portions by the contact line. These are, namely (1) V_1 which is the volume between the meniscus and the contact line and (2) V_2 which is that between the contact line and the surface of the spherical pore.

While the volumes of the emerging droplet in the first two regimes are function of the contact angle (i.e., $V = V(\vartheta)$), it is in the third regime more complex. However, it can be casted as a function of the location of the contact line, x, as shown in Fig. 5b and c. In this case, we have

$$V_1(x) = \frac{\pi}{3} R_p^3 \left\{ \frac{\cos \alpha(x)}{\cos [\vartheta_s - \alpha(x)]} \right\}^3 \left\{ 2 + 3 \sin [\vartheta_s - \alpha(x)] - \sin^3 [\vartheta_s - \alpha(x)] \right\} \quad (15)$$

$$V_2(x) = \frac{\pi}{6} (x - L_1) \left\{ 3 [R_p \cos \alpha(x)]^2 + 3R_t^2 + (x - L_1)^2 \right\} \quad (16)$$

where $\alpha(x)$ is the angle of tangency along the pore profile, x is the location of the contact line, R_p is the radius of the pore, ϑ_s

$$V_2 = \frac{1}{6}\pi(x - L_1)\left\{3(R_p \cos \alpha)^2 + 3R_t^2 + (x - L_1)^2\right\} \tag{17}$$

The spherical profile of the pore may be described as $(x - a)^2 + y^2 = R_p^2$, where a is the location of the center of the pore. The angle of tangency of the pore profile with the x-axis, α, may be determined knowing the slope, which is $dy/dx = -(x - a)/\sqrt{R_p^2 - (x - a)^2}$.

Furthermore, the radius of curvature of the meniscus is related to that of the pore radius as $R_m = R_p \cos \alpha(x)/\cos \beta$, where $\beta(x) = \alpha(x) - \vartheta_s$ with $\alpha(x) = \tan^{-1} dy/dx$. The volume of the emerging droplet in regime III is $V = V_1 + V_2$, from which an equation for updating the location of the contact line may be obtained

$$\frac{\pi}{3V}\left[\frac{R_p \cos \alpha}{\cos(\alpha - \vartheta_s)}\right]^3 [2 + 3\sin(\alpha - \vartheta_s) - \sin^3(\alpha - \vartheta_s)]$$
$$+ \frac{\pi}{6V}(x - L_1)\left\{3(R_p \cos \alpha)^2 + 3R_t^2 + (x - L_1)^2\right\} - 1 = 0 \tag{18}$$

Equation (18) together with those given in Table 1 is used along with Eq. (14) to update the state of the system. It is to be noted that as the meniscus advances inside the pore, it reaches a state in which it becomes flat. Beyond this turning point, in this work, it is assumed that it will continue flat thereafter until it reaches the exit. While this may not be quite accurate, it seems to be a reasonable assumption as will be shown later in the CFD work. Figure 6 shows a schematic that depicts the flat interface and the related dimensions. In this situation, Eq. (14) modifies to

$$(\lambda L_1 + L_2)\frac{8\mu_2}{\pi R_t^4}\frac{dV}{dt} = (p_0 - p_e) \tag{19}$$

Likewise the volume of the invading nonwetting fluid changes linearly with time according to

Fig. 6 Schematic of the interface configuration when it becomes flat
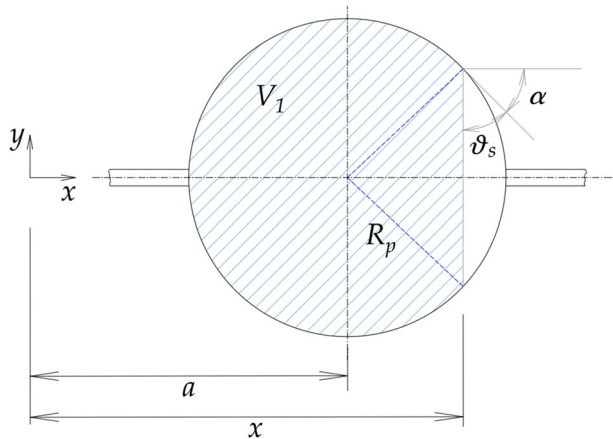
$$V = \frac{p_0 - p_e}{\left(\lambda L_1 + L_2\right)\frac{8\mu_2}{\pi R_t^4}}\left(t - t_c\right) + V_c \tag{20}$$

where V_c is the volume of the nonwetting fluid when the interface becomes flat and t_c is the time when this has happened. The location of the interface thereafter is updated by solving the following quadratic equation at every time step.

$$\frac{\pi}{6V}\left(x - L_1\right)\left\{3\left(R_p\cos\alpha\right)^2 + 3R_t^2 + \left(x - L_1\right)^2\right\} - 1 = 0 \tag{21}$$

3.3 A Numerical Algorithm

Equation (14) may be casted in the following two forms, the difference between them is in the calculation of the radius of curvature, which, in the first form, is a function of the contact angle and in the second form is a function of the location of the contact line.

(a) For regimes I and II

$$\frac{dV(t)}{dt} = \frac{\left[\left(p_0 - p_e\right) - \frac{2\gamma}{R_m(\vartheta(t),t)}\right]}{\left(\lambda L_1 + L_2\right)\frac{8\mu_2}{\pi R_t^4}} \tag{22}$$

(b) For regime III

$$\frac{dV(t)}{dt} = \frac{\left(p_0 - p_e\right) - \frac{2\gamma}{R_m(x(t),t)}}{\left(\lambda L_1 + L_2\right)\frac{8\mu_2}{\pi R_t^4}} \tag{23}$$

This equation represents a nonlinear ode that would be solved numerically. A fourth-order Runge–Kutta method is employed for solving this equation. With $V = V(t)$, the slope of this function at the current time, k_1, at time $t + \Delta t/2$ (i.e., k_2 and k_3), and at time $t + \Delta t$ (i.e., k_4).

$$k_1 = f\left(t_n, V_n\right) \tag{24}$$

$$k_2 = f\left(t_n + \frac{\Delta t}{2}, V_n + \frac{\Delta t}{2}k_1\right) \tag{25}$$

$$k_3 = f\left(t_n + \frac{\Delta t}{2}, V_n + \frac{\Delta t}{2}k_2\right) \tag{26}$$

$$k_4 = f\left(t_n + \Delta t, V_n + \Delta t k_3\right) \tag{27}$$

From which the volume is updated as

$$V(t + \Delta t) = V(t) + \frac{\Delta t}{6}\left(k_1 + 2k_2 + 2k_3 + k_4\right) \tag{28}$$

From the updated volume, all the other variables can be updated.

4 CFD Simulation

CFD simulations have also been conducted to confirm the proposed fates and to provide a framework for comparisons. A computational domain similar to that depicted in Fig. 3 is established in which a spherical pore body is connected to two cylindrical pore throats. In the next few sections, information about the governing equations, the computational setup and the modeling approach, and analysis of the results are provided.

4.1 Governing Equations

Volume of fluid model, as formulated in ANSYS Fluent, has been adopted in this work. It is a finite volume approach for simulating multiphase flow systems where the interfaces are tracked. Even though the equations governing this model along with the Navier–Stokes and continuity equations have been described in several previous works (Salama 2021b, 2022, 2021c, 2021d; Salama et al. 2024, 2023, 2022a, 2022b), for the sake of completion, we briefly list them here. It is to be noted that this system is modeled in the realm of a single heterogeneous fluid system in which the fluid properties are function of space and time. Therefore, there exists a single set of equations of continuity and momentum along with equations to track the interface. These equations can be summarized as.

- Continuity

$$\frac{\partial \rho}{\partial t} + \nabla \cdot \rho \mathbf{v} = 0 \tag{29}$$

where $\mathbf{v}$ is the velocity vector, ρ is the density of the combined systems.

- Momentum

$$\frac{\partial \rho \mathbf{v}}{\partial t} + \nabla \cdot \rho \mathbf{v}\mathbf{v} = -\nabla p + \nabla \cdot \mu \left(\nabla \mathbf{v} + \nabla \mathbf{v}^T \right) + \rho \mathbf{g} + \mathbf{F}_\gamma \tag{30}$$

where $\mathbf{g}$ is the gravity, and $\mathbf{F}_\gamma$ is the interfacial tension force per unit volume, which is nonzero only at the cells located along the interface. This force is calculated as

$$\mathbf{F}_\gamma = \gamma \frac{\rho \kappa \nabla \varphi}{\frac{\rho_1 + \rho_2}{2}} \tag{31}$$

where γ is the interfacial tension, ρ_1 and ρ_2 are the densities of the two phases, κ is the curvature of the interface, and φ is a binary function that defines the phases (i.e., $\varphi = 1$ in the dispersed phase and 0 in the continuous one). The motion of the interface is governed by the solution of a continuity equation for the volume fraction of one (or more) of the phases, e.g., the dispersed phase. That is

$$\frac{1}{\rho} \left[\frac{\partial \rho \varphi}{\partial t} + \nabla \cdot \rho \varphi \mathbf{v} \right] = 0 \tag{32}$$

The curvature, κ is the calculated using

$$\kappa = \frac{1}{|\mathbf{n}|} \left[\left(\frac{\mathbf{n}}{|\mathbf{n}|} \cdot \nabla \right) |\mathbf{n}| - (\nabla \cdot \mathbf{n}) \right] \tag{33}$$

where $\mathbf{n} = \nabla\varphi/|\nabla\varphi|$, is the outwardly unit normal vector. According to the above relationship, a reconstruction of the interface is needed in order to update the configuration of the two phases. One of the most commonly used methods employs piecewise linear interface construction (PLIC) methodology. In this method linear elements are used to describe the volume fraction within each control volume.

4.2 Computational Setup and Analysis

Because of the axisymmetric nature of the setup, a two-dimensional slice has been considered (i.e., axisymmetric system). The computational domain has been discretized into approximately 17,000 quadrilateral-dominant elements. The parameters, dimensions, and boundary conditions relevant to this work are listed in Table 2.

The residuals for all the variables have been set to 10^{-4}, along with an adaptive time stepping scheme. The time step ranges between 10^{-8} and 10^{-6} s for a total simulation time on the order of 5.0 ms. The simulation data obtained from the conducted CFD works are presented as snapshots of the meniscus at different times, pressure profile along the centerline, the pressure history at the inlet and exit of the pore, the volume of the nonwetting fluid in the pore, and the mean velocity in the capillary tubes, as will be described in the next sections.

Figure 7 (Multimedia available online) shows snapshots of the two-phase system at different times for the case in which the contact angle is 135°. The initial condition depicts the system when the nonwetting fluid fills half of the left-hand side capillary tube (Fig. 7a). The interface advances along the tube (Fig. 7b) and eventually pins at the tube exit (Fig. 7c–e). During this time the meniscus develops with its radius of curvature decreasing initially then increasing. Once the contact angle with the tangent to the pore surface at the entrance becomes equal to the static contact angle, the contact line starts to depart the tube exit moving along the pore surface as shown in Fig. 7f–m. As the meniscus advances its radius of curvature increases dramatically toward the exit of the pore and becomes infinitely large when it assumes a flat configuration, Fig. 7m. Thereafter, the interface continues assuming relatively flat interface until it exits the pore (Fig. 7n, o). It is to be noted that a bucket of the wetting fluid may be trapped toward the exit of the pore as depicted in Fig. 7p, q.

This may be due to the fact that the contact line reaches the pore exit later than the middle of the meniscus, which may be a feature of capillary-dominated flows. In fact, the Capillary number based on the flux of the nonwetting fluid inside the capillary tube is on the order of ~0.15, (i.e., $Ca < 1$) and is even smaller based on the speed of the meniscus inside the pore. This indicates that the flow is indeed capillary dominated.

Table 2 Dimensions and parameters used in the CFD work

L_1, μm	L_2, μm	$L_{1,\text{in}}$, μm	R_t, μm	R_p, μm	p_0, kPa
10	10	5.0	2.5	25	120
p_{exit}, kPa	μ_1, Pa.s	μ_2, Pa.s	λ, []	γ, N/m	θ
0	0.01	0.001	10	0.05	135°, 150°

a) 1 (0.0 s)

b) 10 (5 μs)

c) 15 (7.38 μs)

d) 20 (12.6 μs)

e) 25 (20.6 μs)

f) 40 (0.076 ms)

g) 50 (0.12 ms)

h) 75 (0.3 ms)

i) 150 (2.25 ms)

j) 200 (2.73 ms)

k) 225 (2.98 ms)

m) 230 (3.2 ms)

n) 240 (3.4 ms)

o) 260 (3.56 ms)

p) 270 (3.61 ms)

q) 280 (3.78 ms)
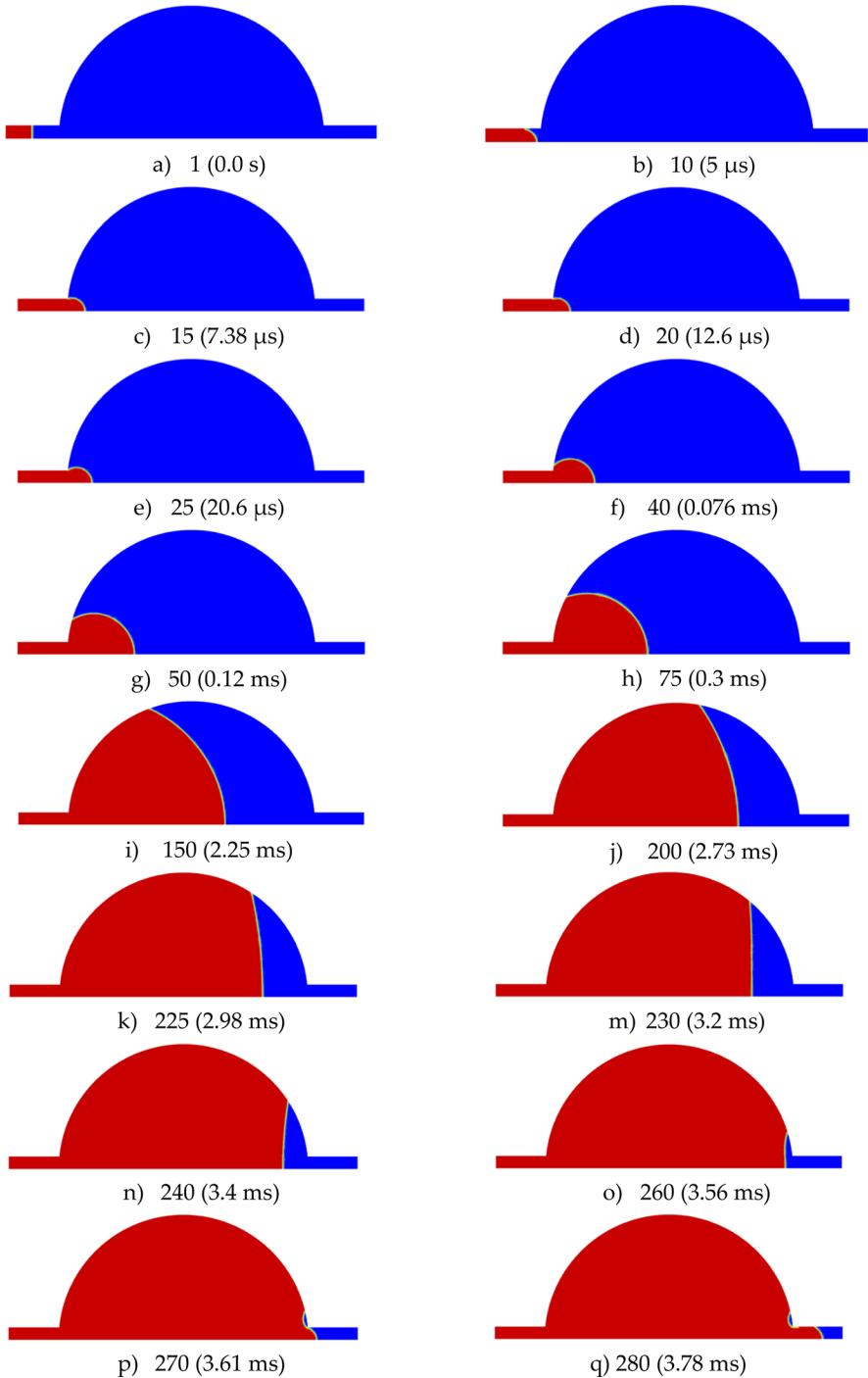
Fig. 7 Snapshots showing the location of the meniscus at different times for the case in which the contact angle is 135°. As the meniscus advances inside the pore, its curvature decreases leading to a decrease in the capillary pressure

The pressure profile along the centerline at different times are depicted in Fig. 8 for the case in which the contact angle is 150°. As depicted, the pressure drops along the left-hand side tube until the meniscus is encountered across which the pressure sharply drops (Fig. 8a). As the meniscus moves along the pore wall, the front of the pressure jump, like-wise, moves along the centerline. This pressure jump represents the capillary pressure and as seen it decreases as the meniscus moves. This is an implication of the increase in the radius of curvature of the meniscus. Furthermore, the pressure along the pore body assumes constant variations before and after the jump, which implies that the assumption of neglecting the pressure drop along the pore body may be valid for the considered scenarios. Figure 9 depicts the time history of the area-weighted average pressures at the inlet and the exit of the pore body. At the pore inlet, the pressure initially drops as the more viscous nonwetting fluid advances along the inlet capillary tube until the meniscus reaches the inlet of the pore.

Then the pressure at the inlet briefly increases as the interface develops with the radius of curvature decreases corresponding to region "I" shown in Fig. 4. The inlet pressure then drops as the interface moves along the pore with the capillary pressure continues to decrease. At the exit, the pressure follows a similar pattern but the jump is delayed until the meniscus reaches the exit (not considered in the developed model). It is to be noted that, the pressures at both the inlet and the exit of the pore body initially converges to be almost equals when the meniscus has reached the inlet of the pore. This confirms that the pressure drop across the pore body may be neglected, which has been one of the assumptions of the developed model.

On the other hand, Fig. 10 shows the variations of the mean velocity in the inlet capillary tube with time. It can be divided into two main regimes according to the dominant resistance: namely (1) inertia-dominated regime and (2) friction-dominated regime. The inertia-dominated regime depicts the very early time when the system starts to move as a result of the imposed external pressure. During this time, fluid inertia develops the largest resistance. As the time passes and the velocity increases, viscous force, likewise develops and eventually supersedes and takes over the inertial resistance leading the velocity to decrease. The velocity continues to drop at even a larger rate beyond the orange dotted line due to the increase in the capillary pressure (i.e., a decrease in the driving force) until it reaches a minimum. The velocity increases thereafter as a result of the continuous decrease in the capillary pressure (i.e., the increase in the external driving force).

Figure 11 shows the development of the volume of the nonwetting fluid in the pore with time for the case in which the contact angle is 135°. As depicted, the volume continuously increases as the nonwetting fluid continues to invade the pore space (Fig. 11a). Figure 11b shows that at the early stage of the invasion process, the volume of the nonwetting fluid in the pore is zero and eventually starts to increase once the nonwetting fluid reaches the pore.

4.3 Validation

In order to build confidence in the developed model, it is important to validate the model against the results of the CFD work. Figure 12 shows the comparisons of the mean velocities in the capillary tube as calculated using the developed model and the CFD work for the cases in which the contact angles are 135° and 150°. It is to be noted that in the CFD work the meniscus started in the middle of the capillary tube and started to develop toward the entrance of the pore, whereas the developed model simulates the filling of the pore starting with the invading fluid right at the entrance of the pore body.
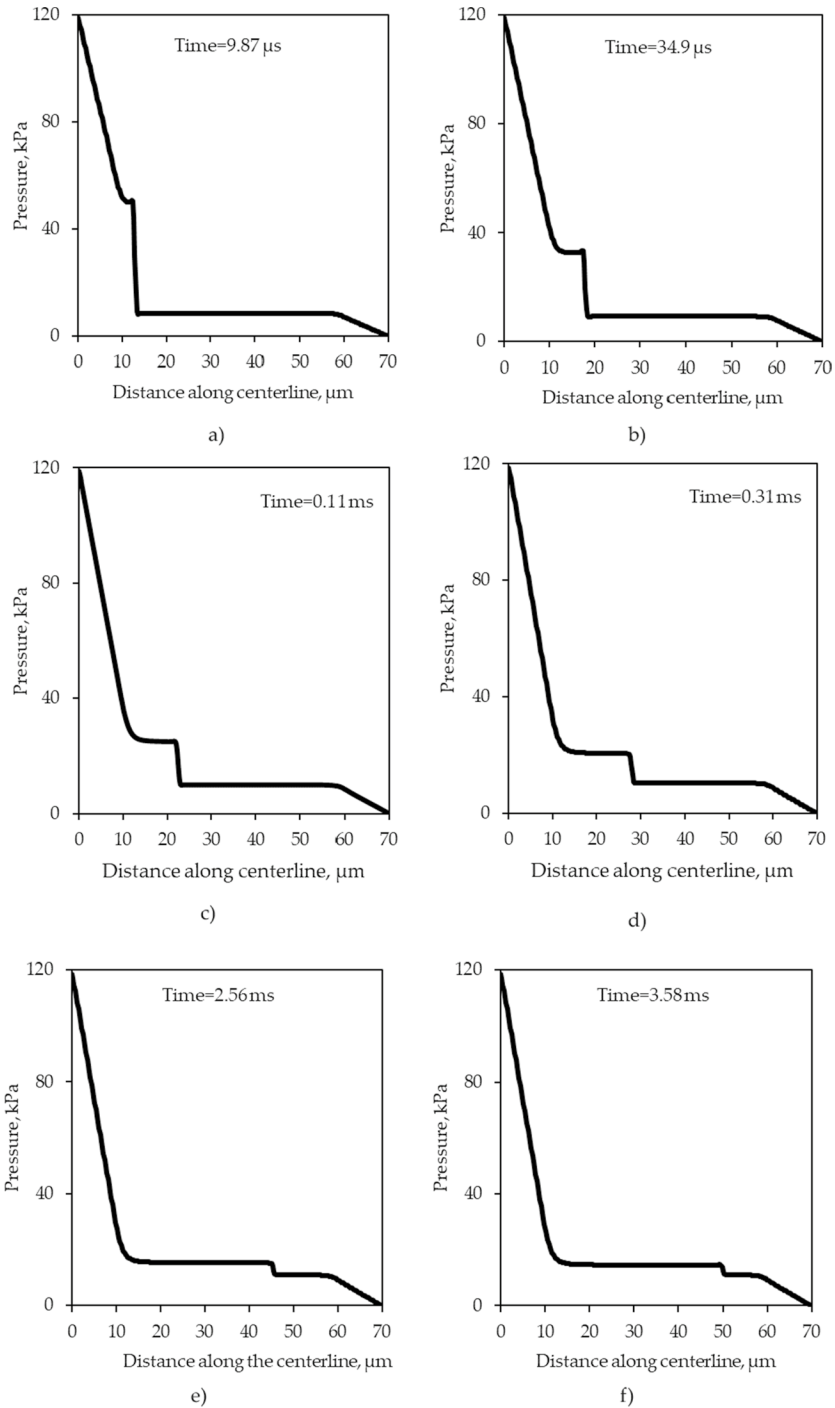
Fig. 8 Pressure profiles along the centerline at different times for the case in which the contact angle is 150°. The pressure jumps across the meniscus and the jump decreases as the meniscus advances inside the pore due to the increase in radius of curvature
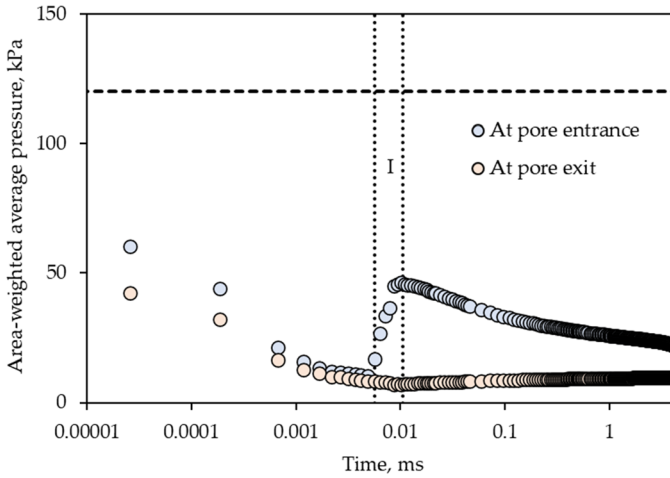
Fig. 9 Variations of the area-weighted average pressures at the entrance and the exit of the pore body with time for the case in which the contact angle is 135°. The vertical dashed lines correspond to the times when the interface has reached the entrance of the pore and started to initially develop according to region "I" shown in Fig. 4 and the horizontal dashed line is the inlet pressure

Fig. 10 The variations of the mean velocity inside the capillary tube variations with time. The vertical lines indicate the onset of important regimes. The first line to the left shows the end of the inertia-dominated regime and the start of the friction-dominated regime. The orange line indicates the arrival of the meniscus at the entrance of the pore, and the left dashed line indicates the start of the movement of the contact line along the profile of the pore body
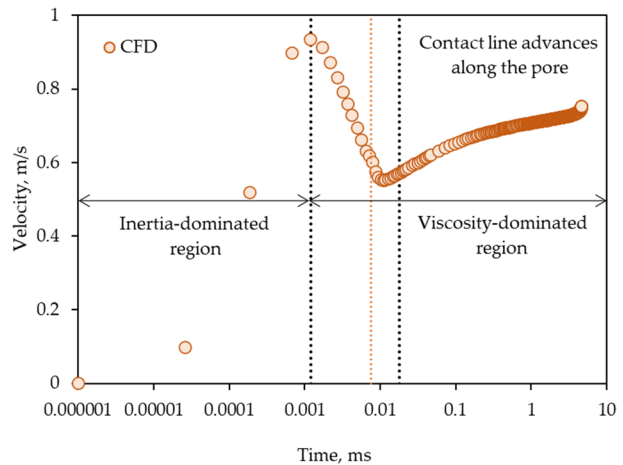
This implies that the data of the model needed to be shifted in time to compare with the CFD work. As shown in Fig. 12a, b, which depict the case in which the contact angle is 135°, generally good match is observed. The model slightly over predicts the velocity, which may be attributed to many things including the neglected friction in the pore body as well as the dynamic effect of the contact angle. On a logarithmic scale, Fig. 12b, the model determination of the velocity follows similar pattern compared with that of the CFD work when the meniscus has pinned at the pore entrance. It initially drops then increases again as the capillary pressure decreases. Similar pattern is also observed for the case in which the contact angle is 150°. It is to be noted that the mean velocity for the 135 scenario is slightly larger than it is for the 135°, which is a manifestation of the fact that the capillary pressure in the former case is slightly smaller than in the latter.
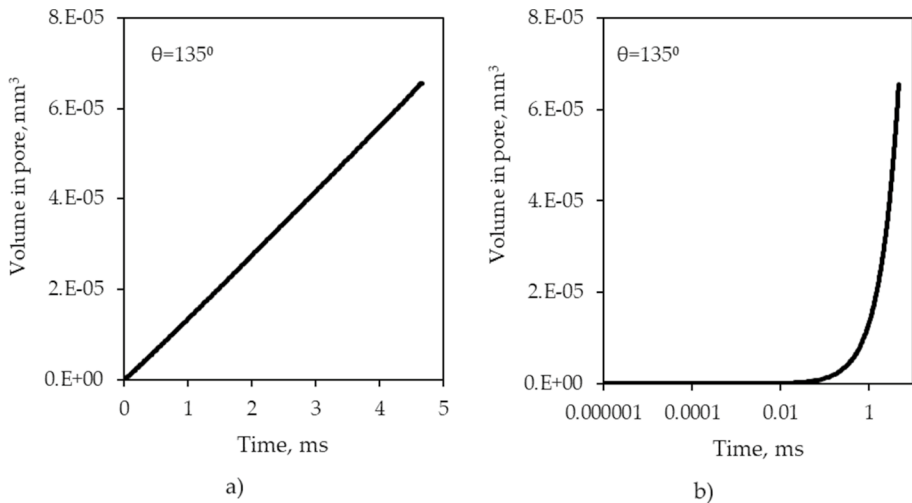
Fig. 11 The variation of the volume of the nonwetting phase inside the pore with time

Figure 13 shows comparisons of the volume of the nonwetting fluid invading the pore with time for the two wetting scenarios, i.e., the 135° scenario (Fig. 13a) and the 150° scenario (Fig. 13b) as calculated using the developed model and the CFD work with both of them showing a very good match.

5 Discussion

Once the model has been validated, it is important that we proceed to investigate other variables. A new scenario of the invading fluid with a contact angle of 135 has been simulated. In this section, a brief illustration of some other variables that the model can provide, which shed light on the behavior of the filling process is given. These variables include, the variations of the total volume of the nonwetting fluid with time, the portion of the total volume between the contact line and the meniscus, and the volume between the contact line and the surface of the pore, the location of the contact line, the radius of curvature of the meniscus, the contact angle, and the angle of tangency of the tube profile.

Figure 14 shows the three volumes mentioned before comprising the invading fluid. As depicted, the volume of the invading fluid linearly increases with time, whereas, the volume underneath the meniscus to the contact line ($V1$) increases at first then drops afterwords. The volume between the pore surface and the contact line (i.e., $V2$) increases nonlinearly, such that the sum of these two volumes equals the total volume. Figure 15 shows the variations with time of the radius of curvature of the meniscus and the location of the contact line. As seen, the radius of curvature increases sharply toward the end implying that the interface becomes flatter. The location of the contact line as the meniscus advances increases in a nonlinear fashion. Finally, Fig. 16 illustrates the changes of both the contact angle and the angle of tangency of the pore profile with time.

In this figure the angle is measured along the axes of symmetry. Both the contact angle and the angle of tangency of the pore profile are parallel once the contact line starts to depart the entrance of the pore (Fig. 16a). However, at the time in which the contact line
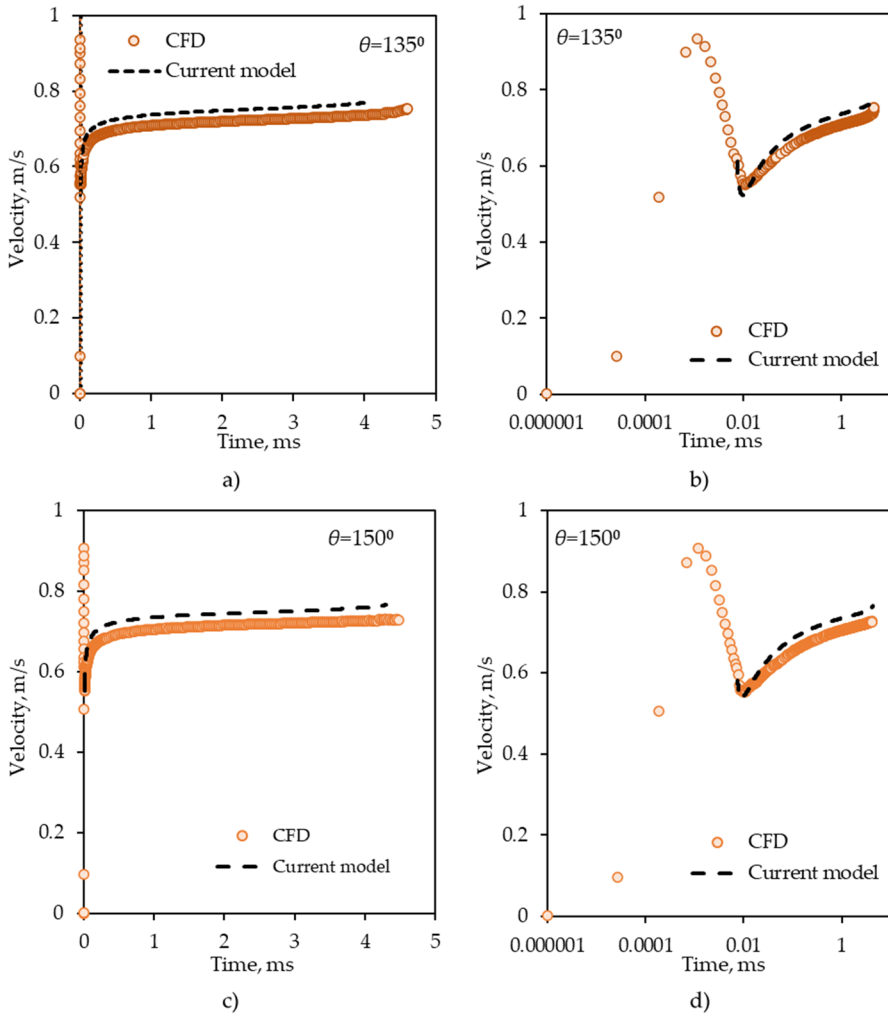
Fig. 12 Comparisons of the mean velocity in the capillary tube between the developed model and the CFD work for the two cases of contact angles (i.e., 135°, and 150°)

pins at the pore entrance, the contact angle first drops to zero, which represents regime I as described before, then starts to increase again until the meniscus assumes the static contact angle with the tangent to the pore profile at the inlet, which marks the end of regime II, as shown in Fig. 16b.

6 Conclusions

In this work, a one-dimensional model is introduced that describes the problem of filling a pore body with a nonwetting invading fluid. This problem finds several applications particularly those related to pore-scale and pore network modeling in porous
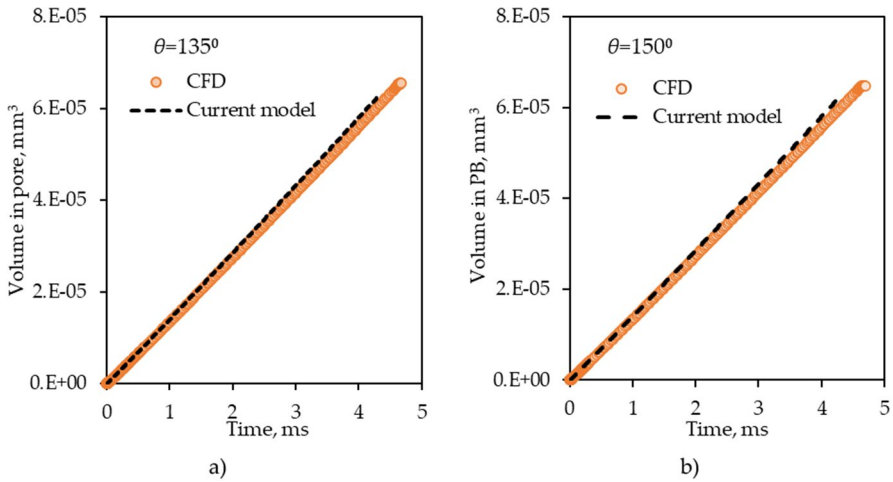
Fig. 13 Comparisons of the variations of the volume of the nonwetting fluid invading the pore with time for the two wetting scenarios as calculated using the developed model and simulated using CFD

Fig. 14 Variations with time of the volume of the fluid in the pore (V), the volume between the contact line and the interface ($V1$), and the volume between the pore body and the contact line, $V2$
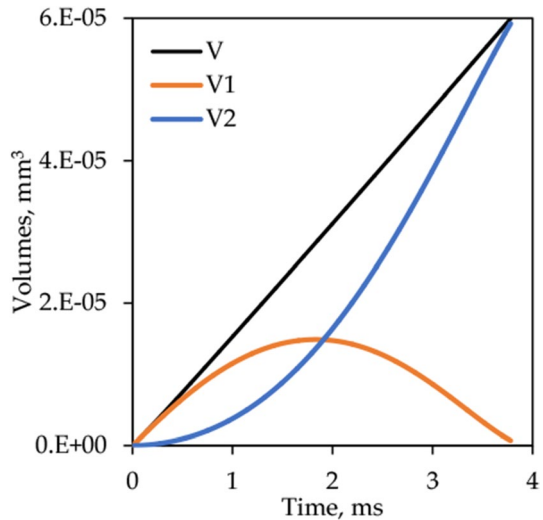
media. The capillary pressure across the developing interface inside the pore plays a pivotal role in dictating the rate of invasion of the nonwetting fluid. This capillary pressure follows interesting patterns. It first briefly increases, reducing, therefore, the rate of invasion, then continuously decreases, increasing, thereby, the rate of invasion. Three regimes have been identified for the developing interface. In the first two regimes, the contact line pins at the entrance of the pore, and in the last one, it departs and moves along the surface of the spherical pore. During the first two regimes, the contact angle develops until it assumes the static one with the tangent to the surface of the pore at the entrance, at which time the contact line starts to depart the pore entrance. As the meniscus advances inside the pore, its radius of curvature increases and eventually becomes

Fig. 15 Variations with time of the radius of curvature of the meniscus, R_m, and the location of the contact line, x

a)

b)
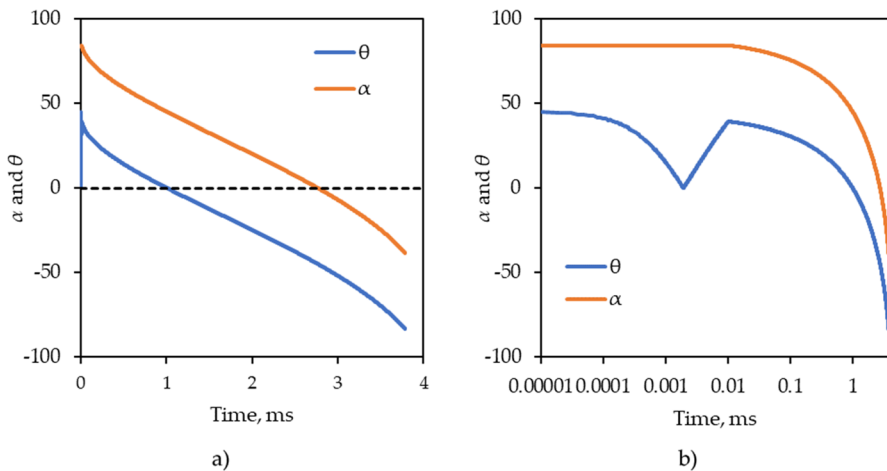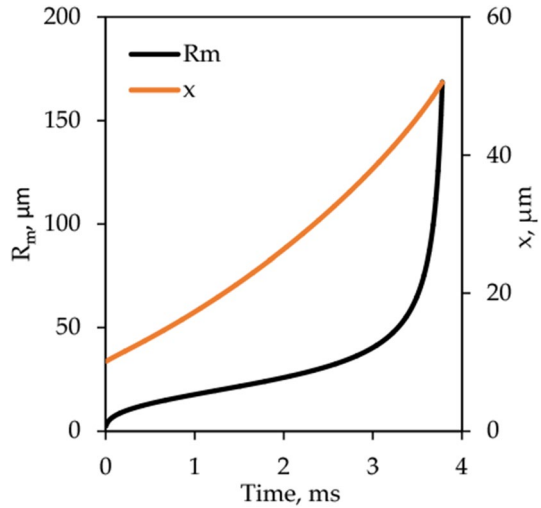
Fig. 16 variations with time of the contact angle, θ, and the angle of tangency (α) of the pore profile as measured from the axis of symmetry, x. The contact angle variations are almost parallel to that of the tangency of the pore profile once the contact line starts to move along the surface of the pore. When the contact line pins at the pore entrance, the contact angle first drops to zero, then increases again

infinitely large indicating the interface becomes flat toward the exit of the pore. The model accounts for all these regimes and also for a wide spectrum of viscosity contrasts of the two immiscible fluids. It generates interesting information about, for example, the location of the contact line, the volume of the invading fluid in the pore (i.e., the saturation), the radius of curvature of the meniscus, the capillary pressure, the contact angle, and others. A CFD analysis has also been conducted to provide a framework for comparisons and validation of the developed model and also to confirm the findings of the model. Comparisons between the model results and the averaged data of the CFD show that the model can predict the dynamicity of the system very well. The developed

model, therefore, can be used to test the assumptions pertinent to the pore network models and help understand the effect of the different parameters.

Data Availability All the data needed to conduct the simulation are included in the manuscript. The CFD work was done by the commercial software ANSYS 2023R2.

Declarations

Conflict of interest The authors have not disclosed any conflict of interest.

References

Adler, P., Thovert, J.-F.: Real porous media: local geometry and macroscopic properties. Appl. Mech. Rev. **51**(9), 537–585 (1998)

Bowen Ling, B., Battiato, I.: τ-SIMPLE algorithm for the closure problem in homogenization of stokes flows. Adv. Water Resour. **144**, 103712 (2020)

Bryant, S.L., Blunt, M.J.: Prediction of relative permeability in simple porous media. Phys. Rev. A **46**(4), 2004 (1992)

Bryntesson, L.M.: Pore network modelling of the behaviour of a solute in chromatography media: transient and steady-state diffusion properties. J. Chromatogr. A **945**(1), 103–115 (2002)

Buckinx, G., Baelmans, M.: Multi-scale modelling of flow in periodic solid structures through spatial averaging. J. Comput. Phys. **291**, 34–51 (2015)

Castro, I.P., Vanderwel, C.: Turbulent Flows: An Introduction. Iop Publishing Ltd, Bristol (2022)

Chabanon, M., Valdés-Parada, F.J., Ochoa-Tapia, J.A., Goyeau, B.: Large-scale model of flow in heterogeneous and hierarchical porous media. Adv. Water Resour. **109**, 41–57 (2017)

Cui, R., Hassanizadeh, S.M., Sun, S.: Pore-network modeling of flow in shale nanopores: network structure, flow principles, and computational algorithms. Earth Sci. Rev. **234**, 104203 (2022). https://doi.org/10.1016/j.earscirev.2022.104203

Das, D.B., Hassanizadeh, S.M.: Upscaling Multiphase Flow in Porous Media: From Pore to Core and Beyond. Springer, Berlin (2005)

El-Amin, M.F., Salama, A., Su, S.: Solute Transport with Chemical Reaction in Single and Multiphase Flow in Porous Media. In: El-Amin, M. (ed.) Mass Transfer in Multiphase Systems and Its Applications. IntechOpen, London (2011)

Fenwick, D., Blunt, M.J.: Network modeling of three-phase flow in porous media. SPE J. **3**(1), 86–96 (1998)

Gao, S., Meegoda, J.N., Hu, L.: Two methods for pore network of porous media. Int. J. Numer. Anal. Methods Geomech. **36**(18), 1954–1970 (2012)

Hefny, M., Qin, C.Z., Saar, M.O., Ebigbo, A.: Synchrotron-based pore-network modeling of two-phase flow in Nubian sandstone and implications for capillary trapping of carbon dioxide. Int. J. Greenhouse Gas Control **103**, 103164 (2020)

Hilpert, M., Miller, C.T.: Pore-morphology-based simulation of drainage in totally wetting porous media. Adv. Water Resour. **24**(3–4), 243–255 (2001)

Hornung, U.: Homogenization and Porous Media, 1st edn. Springer, New York (1997)

Hui, M.H., Blunt, M.J.: Effects of wettability on three-phase flow in porous media. J. Phys. Chem. B **104**(16), 3833–3845 (2000)

Ioannidis, M., Chatzis, I.: On the geometry and topology of 3D stochastic porous media. J. Colloid Interface Sci. **229**(2), 323–334 (2000)

Jivkov, A.P., Xiong, Q.: A network model for diffusion in media with partially resolvable pore space characteristics. Transp. Porous Media **105**(1), 83–104 (2014)

Joekar-Niasar, V., Hassanizadeh, S.M.: Analysis of fundamentals of two-phase flow in porous media using dynamic pore-network models: a review. Crit. Rev. Environ. Sci. Technol. **42**(18), 1895–1976 (2012)

Joekar-Niasar, V., Hassanizadeh, S.M., Dahle, H.K.: Non-equilibrium effects in capillarity and interfacial area in two-phase flow: Dynamic pore-network modelling. J. Fluid Mech. **655**, 38–71 (2010)

Joekar-Niasar, V., van Dijke, M.I.J., Hassanizadeh, S.M.: Pore-scale modeling of multiphase flow and transport: achievements and perspectives. Transp Porous Med. **94**, 461–464 (2012)

Knackstedt, M.A., Sheppard, A.P., Pinczewski, W.: Simulation of mercury porosimetry on correlated grids: evidence for extended correlated heterogeneity at the pore scale in rocks. Phys. Rev. E **58**(6), R6923 (1998)

Laudone, G.M., Matthews, G.P., Gane, P.A.C.: Modelling diffusion from simulated porous structures. Chem. Eng. Sci. **63**(7), 1987–1996 (2008)

Levitz, P.: Off-lattice reconstruction of porous media: critical evaluation, geometrical confinement and molecular transport. Adv. Colloid Interf. Sci. **76**, 71–106 (1998)

Man, H., Jing, X.: Network modelling of wettability and pore geometry effects on electrical resistivity and capillary pressure. J. Pet. Sci. Eng. **24**(2), 255–267 (1999)

Mei, C.C.: Method of homogenization applied to dispersion in porous media. Transp. Porous Med. **9**(3), 261–274 (1992)

Meyers, J., Liapis, A.: Network modeling of the convective flow and diffusion of molecules adsorbing in monoliths and in porous particles packed in a chromatographic column. J. Chromatogr. A **852**(1), 3–23 (1999)

Meyers, J., Nahar, S., Ludlow, D., Liapis, A.I.: Determination of the pore connectivity and pore size distribution and pore spatial distribution of porous chromatographic particles from nitrogen sorption measurements and pore network modelling theory. J. Chromatogr. A **907**(1), 57–71 (2001)

Mohammadmoradi, P., Kantzas, A.: Pore-scale permeability calculation using CFD and DSMC techniques. J. Petrol. Sci. Eng. **146**, 515–525 (2016)

Oren, P.E., Bakke, S.: Process based reconstruction of sandstones and prediction of transport properties. Transp. Porous Media **46**(2–3), 311–343 (2002)

Piller, M., Schena, G., Nolich, M., Favretto, S., Radaelli, F., Rossi, E.: Analysis of hydraulic permeability in porous media: from high resolution X-ray tomography to direct numerical simulation. Transp. Porous Media **80**(1), 57–78 (2009)

Pilotti, M.: Reconstruction of clastic porous media. Transp. Porous Media **41**(3), 359–364 (2000)

Piri, M., Blunt, M.J.: Three-dimensional mixed-wet random pore-scale network modeling of two-and three-phase flow in porous media. I. Model description. Phys. Rev. E **71**(2), 026301 (2005)

Raoof, A., Hassanizadeh, S.M.: A new method for generating pore network models of porous media. Transp. Porous Media **81**(3), 391–407 (2010)

Roberts, A., Torquato, S.: Chord-distribution functions of three-dimensional random media: approximate first-passage times of gaussian processes. Phys. Rev. E **59**(5), 4953 (1999)

Ryazanov, A.V., Van Dijke, M.I.J., Sorbie, K.S.: Two-phase pore-network modelling: existence of oil layers during water invasion. Transp. Porous Media **80**(1), 79–99 (2009)

Salama, A.: Velocity profile representation for fully developed turbulent flows in pipes: a modified power law. Fluids **6**(10), 369 (2021a). https://doi.org/10.3390/fluids6100369

Salama, A.: Imbibition and drainage processes in capillaries: a generalized model, effect of inertia, and a numerical algorithm. Phys. Fluids **33**(8), 10 (2021b)

Salama, A.: A generalized analytical model for estimating the rate of imbibition/drainage of wetting/non-wetting fluids in capillaries. Chem. Eng. Sci. **243**, 116788 (2021c)

Salama, A.: On the coalescence of an oil droplet with a permeating one over a membrane surface: conditions of permeation, recoil, and pinning. Langmuir **37**(12), 3672–3684 (2021d)

Salama, A.: On the estimation of the size of a droplet emerging from a pore opening into a crossflow field. Soft Matter **18**, 1920–1940 (2022)

Salama, A., Van Geel, P.J.: Flow and solute transport in saturated porous media: 1. The continuum hypothesis. J. Porous Media **11**(4), 403–413 (2008)

Salama, A., Van Geel, P.J.: Flow and solute transport in saturated porous media: 2. Violating the continuum hypothesis. J. Porous Media **11**(5), 421–441 (2008)

Salama, A., Zoubeik, M., Henni, A.: A multicontinuum approach for the problem of filtration of oily water systems across thin flat membranes: I. The Framework. AIChE J. **63**(10), 4604–4615 (2017a)

Salama, A., El Amin, M.F., Kumar, K., Sun, S.: Flow and transport in tight and shale formations: a review. Geofluids (2017b). https://doi.org/10.1155/2017/4251209

Salama, A., Van Geel, P., Kou, J., Husein, M.: Investigation of the different regimes associated with the growth of an interface at the exit of a capillary tube into a reservoir: analytical solutions and CFD validation. Langmuir **38**(33), 10274–10287 (2022a)

Salama, A., Kou, J., Alyan, A., Husein, M.: Capillary-driven ejection of a droplet from a micropore into a channel: a theoretical model and a computational fluid dynamics verification. Langmuir **38**(14), 4461–4472 (2022b)

Salama, A., Kou, J., Dawoud, B., Rady, M., El Morshedy, S.: Investigation of the self-propulsion of a wetting/nonwetting ganglion in tapered capillaries with arbitrary viscosity and density contrasts. Colloids Surf. A **664**, 131151 (2023)

Salama, A., Kou, J., Dawoud, B., Simonson, C.: A modeling approach for capillary-driven flow of a wetting fluid in a rectangular open microchannel of arbitrary axisymmetric width profile: application to heat pipes. Int. J. Therm. Sci. **195**, 108622 (2024)

Silin, D., Tomutsa, L., Benson, S.M., Patzek, T.W.: Microtomography and pore-scale modeling of two-phase fluid distribution. Transp. Porous Media **86**(2), 525–545 (2011)

Thompson, K.E.: Pore-scale modeling of fluid transport in disordered fibrous materials. AIChE J. **48**(7), 1369–1389 (2002)

Whitaker, S.: The Method of Averaging. Springer, Dordrecht (1999)

Wood, B.D., Cherblanc, F., Quintard, M., Whitaker, S.: Volume averaging for determining the effective dispersion tensor: closure using periodic unit cells and comparison with ensemble averaging. Water Resour. Res. **39**, 8 (2003). https://doi.org/10.1029/2002WR001723

Yeong, C., Torquato, S.: Reconstructing random media. Phys. Rev. E **57**(1), 495 (1998)

Yin, X., de Vries, E.T., Raoof, A., Hassanizadeh, S.M.: Dynamic Pore-Network Models Development. In: Singh, V., Gao, D., Fischer, A. (eds.) Advances in Mathematical Methods and High-Performance Computing, vol. 41, pp. 1–5. Springer, Cham (2019)

Zhang, T., Salama, A., Sun, S., El Amin, M.F.: Pore network modeling of drainage process in patterned porous media: a quasi-static study. J. Comput. Sci. **9**, 64–69 (2025)

Authors and Affiliations

Amgad Salama[1] ⬦ · **Jisheng Kou**[2,3] · **Shuyu Sun**[4] · **Mahmoud Hefny**[5]

✉ Amgad Salama
   asas.tx@gmail.com

[1] Mechanical Engineering Department, University of Saskatchewan, Saskatoon, SK S7N 5A9, Canada

[2] School of Civil Engineering, Shaoxing University, Shaoxing 312000, Zhejiang, China

[3] School of Mathematics and Statistics, Hubei Engineering University, Xiaogan 432000, Hubei, China

[4] Computational Transport Phenomena Laboratory, Physical Science and Engineering Division, King Abdullah University of Science and Technology, 23955-6900 Thuwal, Kingdom of Saudi Arabia

[5] Geothermal Energy and Geofluids, Department of Earth Sciences, ETH Zurich, Zurich, Switzerland